

Optical and transport anisotropies in spin-textured altermagnets

Andrea Maiani¹

¹ *Nordita, KTH Royal Institute of Technology and Stockholm University,
Hannes Alfvéns väg 12, SE-10691 Stockholm, Sweden*

(Dated: February 17, 2026)

Spin textures are ubiquitous in antiferromagnets, yet their consequences for altermagnets remain largely unexplored. We show that spatial variations of the Néel order act on the low-energy electrons as effective gauge fields, leading to strong in-plane anisotropies in both dc transport and optical absorption, even without intrinsic spin-orbit coupling. As a concrete example, we analyze a coplanar spin helix and predict that the principal axes of the conductivity and linear dichroism are set by the helix wave vector and can be tuned by the texture geometry. Our results point to polarization-resolved optics and anisotropic transport as direct probes of textured altermagnetic states, and suggest a simple route to direction-selective electronic and optical functionality in altermagnets.

Altermagnets are antiferromagnetically ordered materials with vanishing net magnetization, where opposite-spin sublattices are related by a crystal symmetry other than a simple real-space translation or inversion [1–7]. This multipolar order breaks time-reversal and crystal-rotation symmetries separately while preserving their combinations, yielding spin-split bands at finite momentum despite zero net magnetization. Experimental signatures have been reported in materials including RuO₂, α -MnTe, and Mn₅Si₃, among others [8–12]. Further candidate platforms and evidence across oxides, chalcogenides, and cuprates are discussed in Refs. [13–17].

A minimal description starts from collinear antiferromagnetic order complemented with hopping processes that do not respect the translation that maps one magnetic sublattice onto the other [18]. At the same time, domain formation and nonuniform Néel configurations are common in antiferromagnets due to the absence of stray fields [19]. Yet, the impact of spin textures on electronic response in altermagnets remains largely unexplored, with only a few recent works addressing texture-driven transport phenomena [20, 21]. Consistent with this expectation, nanoscale probes already indicate nonuniform Néel textures in candidate altermagnets [22, 23].

In this work, we develop an effective theory for electron transport in spin-textured collinear altermagnets. We derive a controlled low-energy theory by projecting the SU(2) gauge-covariant texture coupling onto the altermagnetic doublet, showing that gradients of the Néel order parameter act as emergent gauge fields on the electronic pseudospin [24–28]. This framework yields three generic consequences: a texture-induced pseudospin-orbit coupling, an emergent electromagnetic coupling associated with texture singularities, and a pseudospin splitting accompanied by a chemical-potential renormalization. We illustrate these effects for d-wave and g-wave altermagnets, and, for a spin-helix configuration, we show that the texture wave vector controls both the magnitude and the principal axes of anisotropic optical absorption and transport.

Model – We adopt the minimal two-sublattice description of collinear altermagnets proposed in Ref. 18. In this

setting, the magnetic order enforces anti-alignment of the local moments on the two magnetic sublattices. A spin texture is described by a slowly varying staggered order parameter, the Néel vector $\mathbf{n}(\mathbf{r})$, which defines the local spin quantization axis.

The itinerant electronic Hamiltonian is

$$H = H_{\text{kin}}(\mathbf{k}) - J \mathbf{n}(\mathbf{r}) \cdot \boldsymbol{\sigma} \eta_z, \quad (1)$$

where $\mathbf{k} = (k_x, k_y)$ is the crystal momentum in a two-sublattice (A, B) unit cell, $H_{\text{kin}}(\mathbf{k})$ encodes spin-independent hopping processes, the η_α (σ_i) are Pauli matrices acting in sublattice (spin) space, and J is the exchange coupling. Throughout, we assume $\mathbf{n}(\mathbf{r})$ varies slowly on the lattice scale. Here and throughout the paper we assume $e = \hbar = 1$. In the absence of intrinsic spin-orbit coupling, $H_{\text{kin}}(\mathbf{k}) \propto \sigma_0$ and its sublattice structure are fixed by crystal symmetries. For centrosymmetric crystals, the allowed terms are even in \mathbf{k} .

For explicit calculations, we consider a two-dimensional altermagnet and use a continuum parametrization around an inversion-symmetric point,

$$H_{\text{kin}}(\mathbf{k}) = \frac{k^2}{2m} + \left[C^x + \frac{K^x}{2} k^2 \right] \eta_x + \frac{K_n^z}{n!} g_n(\mathbf{k}) \eta_z, \quad (2)$$

where $\mathbf{k} = (k_x, k_y)$. The parameters m , C^x , K_n^x , and K^z control the isotropic dispersion, sublattice hybridization, and symmetry-allowed staggered anisotropy, respectively. The basis function $g_n(\mathbf{k})$ is odd under sublattice exchange, with $g_2(\mathbf{k}) = k_x k_y$ for the d-wave case and $g_4(\mathbf{k}) = k_x k_y (k_y^2 - k_x^2)$ for the g-wave case.

Before discussing transport, we stress that collinear antiferromagnets and altermagnets can respond quite differently to spin textures, despite both having zero net magnetization. In a conventional collinear antiferromagnet, the Néel vector is effectively headless, i.e., $\mathbf{n} \sim -\mathbf{n}$. Therefore, in the absence of additional symmetry breaking, the electronic Hamiltonian typically does not distinguish a texture from its globally reversed partner. This does not rule out long-lived skyrmion-like textures: even without strict topological protection, exchange stiffness and anisotropy can yield large activation barriers and long

lifetimes on experimental time scales [29]. In altermagnets, by contrast, the electronic structure can distinguish \mathbf{n} from $-\mathbf{n}$, making observables sensitive to the texture's chirality [20, 30]. While this does not make the skyrmion winding number strictly protected, it does mean that textures can generate emergent gauge fields with experimentally accessible signatures, closely analogous to texture-induced Berry-phase effects in ferromagnets [25, 31].

We treat an inhomogeneous Néel texture $\mathbf{n}(\mathbf{r})$ using a local unitary $U(\mathbf{r}) \in \text{SU}(2)$ that aligns the spin quantization axis with the exchange field [24–28] such that

$$U^\dagger(\mathbf{r}) \mathbf{n}(\mathbf{r}) \cdot \boldsymbol{\sigma} U(\mathbf{r}) = \sigma_z, \quad (3)$$

Spatial gradients generate a non-Abelian connection

$$\mathcal{A}_j \equiv -i U^\dagger \partial_j U \equiv \frac{1}{2} \mathbf{A}_j \cdot \boldsymbol{\sigma}, \quad D_j \equiv \partial_j + i \mathcal{A}_j, \quad (4)$$

so that the exchange field becomes uniform, while the kinetic energy couples to the texture through $-i\partial_j \rightarrow -iD_j$. Because \mathcal{A}_j is matrix valued, operator ordering matters when expanding $H_{\text{kin}}(\mathbf{p})$ in powers of momentum. We define the gauge-coupled kinetic term by Weyl symmetrization, resulting in

$$H = \mathcal{W}[H_{\text{kin}}(k_j \rightarrow -iD_j)] - J \sigma_z \eta_z, \quad (5)$$

where $\mathcal{W}[\cdot]$ denotes full symmetrization over non-commuting covariant derivatives.

The unitary $U(\mathbf{r})$ defines a comoving orthonormal triad $(\mathbf{e}_1, \mathbf{e}_2, \mathbf{e}_3)$ with $\mathbf{e}_3 = \mathbf{n}$, and allows one to decompose the $\text{SU}(2)$ connection into components transverse and longitudinal to \mathbf{n} ,

$$\mathbf{A}_j = \mathbf{A}_j^\perp + A_j^\parallel \mathbf{n}, \quad \mathbf{A}_j^\perp \equiv \mathbf{A}_j - (\mathbf{A}_j \cdot \mathbf{n}) \mathbf{n}, \quad (6)$$

The transverse component is fixed uniquely by the texture,

$$\mathbf{A}_j^\perp = \mathbf{n} \times \partial_j \mathbf{n}, \quad (7)$$

whereas the longitudinal part

$$A_j^\parallel \equiv \mathbf{A}_j \cdot \mathbf{n} = -\mathbf{e}_1 \cdot \partial_j \mathbf{e}_2 \quad (8)$$

is the residual $\text{U}(1)_z$ gauge field (local rotations of $\mathbf{e}_{1,2}$ about \mathbf{n}) and is gauge dependent. Local observables therefore depend only on gauge-invariant combinations, in particular the texture metric

$$g_{jk} \equiv \mathbf{A}_j^\perp \cdot \mathbf{A}_k^\perp = \partial_j \mathbf{n} \cdot \partial_k \mathbf{n}, \quad (9)$$

as well as the leading gradient coupling linear in the transverse connection, of the form $\mathbf{A}_j^\perp \partial_k$. For textures with topological defects, an additional gauge-invariant quantity is the skyrmion density. Additional details are given in Appendix A.

We now focus on the d -wave case ($n = 2$), while the general band-expansion can be found in the Appendix B.

Including the texture through covariant derivatives, the resulting Hamiltonian becomes

$$H_d = C^x \eta_x - \frac{1}{2m} \eta_0 D^2 - \frac{K^x}{2} \eta_x D^2 - \frac{K_d^z}{2} \frac{\eta_z}{2} \{D_x, D_y\} - J \sigma_z \eta_z. \quad (10)$$

where the Weyl symmetrized product reduces to an anticommutator, and it naturally splits into three components:

$$\begin{aligned} \frac{1}{2} \{D_j, D_k\} &= \underbrace{\left(\partial_j + i A_j^\parallel \frac{\sigma_z}{2} \right) \left(\partial_k + i A_k^\parallel \frac{\sigma_z}{2} \right)}_{\text{emergent electromagnetic coupling}} \\ &+ \underbrace{i \left(\mathbf{A}_j^\perp \partial_k + \mathbf{A}_k^\perp \partial_j \right) \cdot \frac{\boldsymbol{\sigma}^\perp}{2}}_{\text{emergent spin-orbit coupling}} - \underbrace{\frac{g_{jk}}{4} \sigma_0}_{\text{scalar potential}}. \end{aligned} \quad (11)$$

The first term represents the *emergent electromagnetic coupling* to the Abelian gauge field A_j^\parallel . The second term represents the *emergent pseudospin-orbit coupling* generated by the transverse texture. Finally, the third line is a *scalar potential* proportional to the texture metric.

We consider the strong-coupling regime where the exchange term defines the dominant energy scale, $J \gg \|H_{\text{kin}}\|$, and treat the kinetic part as a perturbation. Let $P = \frac{1+\sigma_z \eta_z}{2}$ denote the projectors onto the low-energy doublet $\{|A\uparrow\rangle, |B\downarrow\rangle\}$. By projecting into the low-energy section, the resulting effective Hamiltonian reads

$$\begin{aligned} H_{d,\text{eff}} = PH_{\text{kin}}P &= \frac{1}{2m} \left[\sum_{\alpha=x,y} \left(-i D_\alpha^\parallel \right)^2 + \frac{g_{\alpha\alpha}}{4} \tau_0 \right] \\ &+ \frac{K_d^z}{2} \tau_3 \left[-D_x^\parallel D_y^\parallel + \frac{g_{xy}}{2} \tau_0 \right] \\ &- i K^x (\mathbf{A}_x^\perp \partial_x + \mathbf{A}_y^\perp \partial_y) \cdot \frac{\boldsymbol{\tau}}{2}, \end{aligned} \quad (12)$$

where $D_\alpha^\parallel = \partial_\alpha + i A_\alpha^\parallel \frac{\tau_3}{2}$ and we identified the Pauli algebra inside the two-component subspace with the τ_i matrices. A nonzero C_x can be treated nonperturbatively and leads to a renormalization of the coefficient, as derived in Appendix B via Schrieffer-Wolff transformation up to second order in H_{kin} .

Eq. (12) is the main technical result: it provides a compact low-energy description of electrons coupled to an arbitrary smooth Néel texture in a collinear altermagnet. It also highlights the qualitative difference from a conventional collinear antiferromagnet. For an antiferromagnet ($K^z = 0$), the sublattice-odd kinetic channel is absent, and the effective theory contains no τ_3 component, so texture-induced terms remain strictly sublattice even. In that limit, textures can generate a pseudospin-orbit interaction but cannot produce τ_3 -odd electronic signatures. For an altermagnet ($K^z \neq 0$), by contrast, the texture couples to the sublattice-odd channel and generates a local τ_3 contribution controlled by contractions of texture gradients through the metric g_{jk} . Consequently, smooth

textures such as domain walls and spirals can imprint a localized τ_3 signal in sublattice-resolved spectral observables, e.g. the momentum-resolved τ_3 -weighted spectral function.

Spin helix – A coplanar spin helix is one of the simplest and most physically relevant spin textures. It can be realized in antiferromagnets with Dzyaloshinskii-Moriya interactions or under strain gradients that break inversion symmetry, where the competition between exchange and spin-orbit coupling stabilizes spiral Néel configurations even without external fields [32]. We consider a planar helix with propagation wavevector $\mathbf{q} = (q_x, q_y)$ parametrized as

$$\mathbf{n}(\mathbf{r}) = \mathbf{u} \cos(\mathbf{q} \cdot \mathbf{r}) + \mathbf{v} \sin(\mathbf{q} \cdot \mathbf{r}), \quad (13)$$

where \mathbf{u} and \mathbf{v} are fixed orthonormal unit vectors spanning the helix plane, and $\mathbf{w} \equiv \mathbf{u} \times \mathbf{v}$ is the normal to that plane, so that $\mathbf{n} \times \partial_i \mathbf{n} = q_i \mathbf{w}$. Choosing the comoving frame with $\mathbf{e}_1 = \mathbf{w}$ fixes $A_j^{\parallel} = 0$ and $A_j^{\perp} = q_j \mathbf{e}_1$.

In the d -wave case, the long-wavelength Hamiltonian for itinerant electrons reads

$$H_{d,h} = \frac{1}{2m} \left[k_x^2 + k_y^2 + \frac{q_x^2 + q_y^2}{4} \right] + \frac{K^x}{2} \tau_1 (q_x k_x + q_y k_y) + \frac{K^z}{2} \tau_3 \left[k_x k_y + \frac{q_x q_y}{2} \right], \quad (14)$$

while for the g -wave case, up to quadratic order in gradients, the effective Hamiltonian becomes

$$H_{g,h} = \frac{1}{2m} \left[k_x^2 + k_y^2 + \frac{q_x^2 + q_y^2}{4} \right] + \frac{K^x}{2} \tau_1 (q_x k_x + q_y k_y) + \frac{K^z}{24} \tau_3 \left[k_x k_y (k_y^2 - k_x^2) - \frac{3}{16} (g_{xy} (k_x^2 - k_y^2) + (g_{xx} - g_{yy}) k_x k_y) \right]. \quad (15)$$

Both Hamiltonians can be written as $H = d_0 \tau_0 + d_1 \tau_1 + d_3 \tau_3$. The bands are $E_{\pm} = d_0 \pm \sqrt{d_1^2 + d_3^2}$, and the pseudospin polarization is $\langle \tau_j \rangle_{\pm} = \pm d_j / \sqrt{d_1^2 + d_3^2}$. Band touchings require $\mathbf{d} = 0$, i.e., $q_x k_x + q_y k_y = 0$ and $k_x k_y = -\frac{1}{2} q_x q_y$. For helix directions along crystal axes, the continuum model admits symmetry-enforced degeneracy lines that intersect a given Fermi contour at isolated points; away from these special orientations, the helix generically lifts the degeneracy and splits the Fermi surfaces anisotropically.

The maps in Fig. 1 visualize the pseudospin polarization at the Fermi surface, defined as

$$\rho_3(\mathbf{k}, \omega) \equiv \frac{1}{2\pi} \text{Im} \text{Tr} [\tau_3 (G^A(\mathbf{k}, \omega) - G^R(\mathbf{k}, \omega))], \quad (16)$$

where $G^{R,A} = [\omega + \mu - H(\mathbf{k}) \pm i\eta]^{-1}$ are the Green's functions, μ is the chemical potential, and $\eta = 1/(2\tau)$

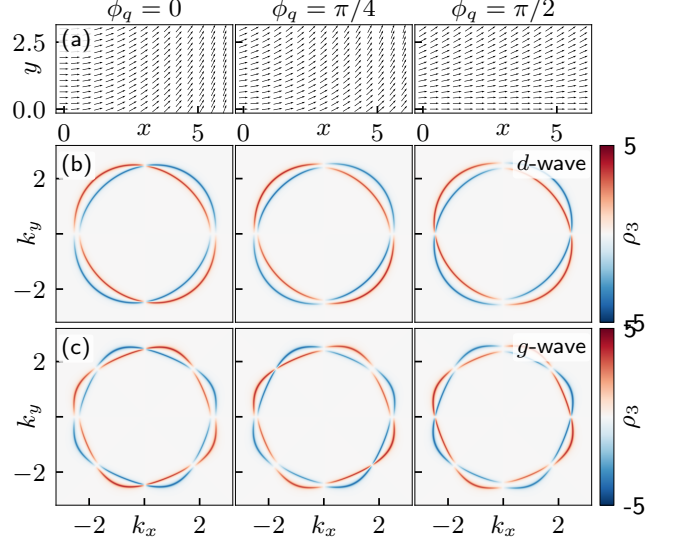


FIG. 1. (a) Real-space spin texture for a planar spin helix with propagation vector $\mathbf{q} = q \cos(\phi_q) \hat{x} + q \sin(\phi_q) \hat{y}$, shown for three helix orientations ϕ_q . Momentum-resolved sublattice-polarized spectral function for a d -wave (b) and g -wave (c) alternatemagnet. Parameters used: $m = 1.0$, $K^x = 1.0$, $q = 0.2$, $\mu = 3$, $\eta = 0.08$, $K_d^z = 0.3$, $K_g^z = 0.9$.

is an effective broadening. Within the effective theory, a smooth helix generates two texture-induced ingredients. First, a universal texture induced pseudospin orbit coupling in the τ_1 channel, which twists the pseudospin texture along the constant energy contour and produces the helix induced Fermi surface splitting. Second, a texture induced staggered potential in the τ_3 channel, which is directly picked up by ρ_3 . The key distinction between the d wave and g wave models is the momentum structure of this τ_3 contribution: in the g wave case, the contraction of the intrinsic $\ell = 4$ anisotropy with the texture metric lowers the effective symmetry and reshapes the response into a mixture of lower harmonics, so the induced τ_3 polarization becomes strongly angle dependent and alternates in sign around the contour rather than producing a uniform splitting.

The longitudinal conductivity in the static limit is evaluated in the Kubo bubble approximation,

$$\sigma_{ij}^{\text{DC}} = -\frac{e^2}{2\pi} \int \frac{d^2 k}{(2\pi)^2} \text{Tr} [v_i(\mathbf{k}) G^R(\mathbf{k}) v_j(\mathbf{k}) G^A(\mathbf{k})], \quad (17)$$

with the bare velocity vertex $v_i(\mathbf{k}) = \partial_{k_i} H(\mathbf{k})$ [33]. This captures the symmetry-allowed anisotropies arising from the band velocities and pseudospin texture; vertex corrections can renormalize the magnitude but do not modify the symmetry of σ_{ij} in the weak-disorder regime.

For a homogeneous Néel state ($q = 0$), tetragonal symmetry enforces $\sigma_{xx} = \sigma_{yy}$. A spin helix lowers the symmetry and unlocks an anisotropic correction whose leading long-wavelength structure is set by the helix metric, $g_{ij} \propto q_i q_j$. It is therefore natural to analyze the response

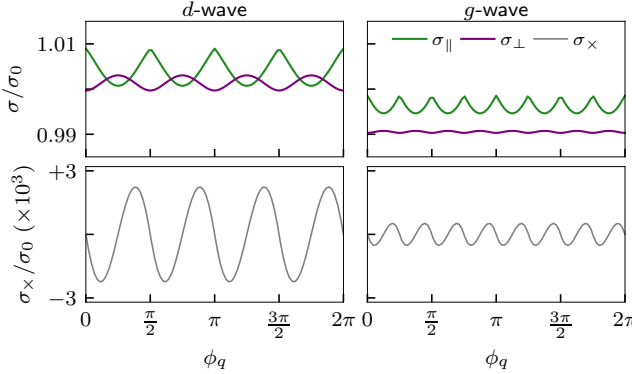


FIG. 2. Helix-orientation dependence of the dc conductivity, shown in the basis defined by the helix direction \hat{q} and its in-plane perpendicular \hat{q}_\perp . Top row: longitudinal components $\sigma_{\parallel} = \hat{q} \cdot \sigma \cdot \hat{q}$ and $\sigma_{\perp} = \hat{q}_\perp \cdot \sigma \cdot \hat{q}_\perp$, normalized to the Drude value $\sigma_0 = \mu\tau/\pi$. Bottom row: off-diagonal component $\sigma_x = \hat{q} \cdot \sigma \cdot \hat{q}_\perp$, which diagnoses any residual misalignment between \hat{q} and the principal axes of the conductivity tensor. Left column: representative *d*-wave altermagnet, showing a pronounced splitting between σ_{\parallel} and σ_{\perp} with a characteristic fourfold ($\pi/2$ -periodic) ϕ_q modulation. Right column: representative *g*-wave altermagnet, where the ϕ_q dependence is strongly reduced in amplitude (with a weak $\pi/4$ -periodic modulation). Here and in the following $\eta = 0.03$ while the other parameters are the same as in Fig. 1.

in the spiral basis defined by \hat{q} and \hat{q}_\perp , with components σ_{\parallel} , σ_{\perp} , and σ_x . As shown in Fig. 2, the *d*-wave model exhibits a clear splitting between σ_{\parallel} and σ_{\perp} together with a pronounced ϕ_q modulation controlled by the tetragonal (d_{xy}) anisotropy of the altermagnetic channel. In contrast, in the *g*-wave model the conductivity is much less sensitive to the helix orientation: σ_{\parallel} and σ_{\perp} are nearly flat as functions of ϕ_q , and the dominant effect is an approximately ϕ_q -independent anisotropic offset. In both cases, σ_x remains subleading, indicating that \hat{q} closely tracks the principal axes of the symmetric conductivity tensor for the parameters shown.

The helix-induced pseudospin texture makes the interband optical matrix elements strongly direction dependent. As a result, the system absorbs light differently depending on the polarization direction within the plane. This polarization-dependent absorption is *linear dichroism*: two orthogonal linear polarizations experience different absorption at the same frequency.

In linear response, absorption is proportional to the dissipative part of the optical conductivity. Equivalently, the real conductivity tensor $\text{Re } \sigma_{ij}(\omega)$ has two in-plane principal values, $\sigma_+(\omega)$ and $\sigma_-(\omega)$, corresponding to its eigenpolarizations. Linear dichroism corresponds to $\sigma_+(\omega) \neq \sigma_-(\omega)$, and in our case, these principal values inherit a characteristic dependence on the helix orientation angle ϕ_q . We quantify the dichroism strength by

$$\mathfrak{D}(\omega) = \frac{\sigma_+(\omega) - \sigma_-(\omega)}{\sigma_+(\omega) + \sigma_-(\omega)}, \quad (18)$$

and define the total absorption as

$$\mathfrak{A}(\omega) = \sigma_+(\omega) + \sigma_-(\omega). \quad (19)$$

The corresponding principal absorption axis $\theta_+(\omega)$ is the eigenvector angle of $M_{ij}(\omega)$.

The optical conductivity is obtained from the standard relation

$$\sigma_{ij}(\omega) = \frac{i}{\omega} [K_{ij}(\omega) - K_{ij}(0)], \quad (20)$$

where $K_{ij}(\omega)$ is the retarded current-current correlator. To analyze anisotropy and symmetry, we focus on the interband paramagnetic contribution, since it encodes the full angular dependence through the off-diagonal optical matrix elements. Specifically, we use

$$K_{ij}^{\text{para}}(\omega) = -e^2 \int d\mathbf{k} \sum_{n \neq m} \frac{f_{n\mathbf{k}} - f_{m\mathbf{k}}}{\omega + i\eta - \Delta_{mn}} v_i^{nm} v_j^{mn}, \quad (21)$$

where $v_i^{nm}(\mathbf{k})$ are the interband velocity matrix elements, $\Delta_{mn} = (E_{m\mathbf{k}} - E_{n\mathbf{k}})$, $f_{n\mathbf{k}} = [e^{E_{n\mathbf{k}}/T} + 1]^{-1}$ are Fermi-Dirac occupation factors at temperature T .

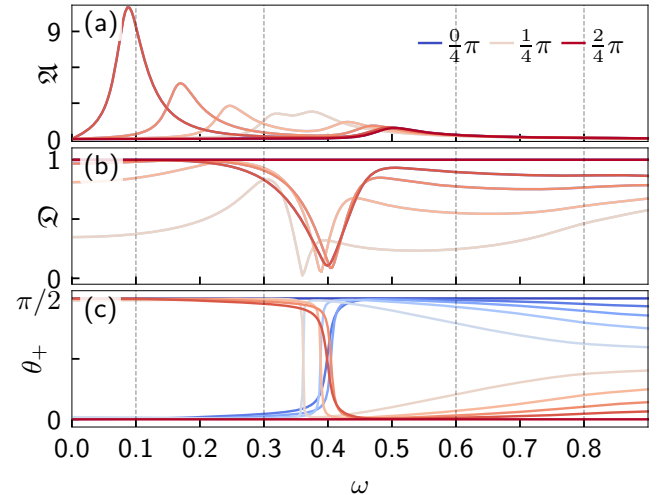


FIG. 3. (a) Total optical absorption $\mathfrak{A}(\omega)$ for different orientations ϕ_q from 0 (red line) to $\pi/2$ (blue line). (b) Corresponding linear dichroism $\mathfrak{D}(\omega)$. (c) Frequency-dependent orientation $\theta_+(\omega)$ of the principal absorption axis (defined modulo π). The vertical dashed line marks the representative frequencies ω_0 used in panel Fig. 4(a).

Since the helix breaks the crystalline C_4 symmetry down to C_2 , the tensor structure of $K_{ij}^{\text{para}}(\omega)$ becomes angle dependent. Specifically, the interband absorption is controlled by the off-diagonal velocity matrix elements

$$v_i^{+-} = \frac{d_3 \partial_{k_i} d_1 - d_1 \partial_{k_i} d_3}{\sqrt{d_1^2 + d_3^2}} \quad (22)$$

which, for the *d*-wave helix with $q \ll k_F$, gives

$$v_i^{+-} \approx -\frac{K^x K^z}{8} \frac{q_i k_i^2}{\sqrt{d_1^2 + d_3^2}}, \quad (23)$$

where $(\bar{x} \equiv y, \bar{y} \equiv x)$. Eq. (23) shows that the optical anisotropy is not trivially locked to \mathbf{q} since x -polarized transitions are controlled by q_y (and vice versa), reflecting interference between the helix-induced mixing through pseudospin-orbit coupling and the crystal form factor.

In conventional collinear antiferromagnets, linear dichroism is commonly discussed as arising from intrinsic spin-orbit and crystal-field anisotropies that couple the optical tensor to the Néel axis. Within a centrosymmetric continuum description without intrinsic spin-orbit coupling, a smooth Néel texture is not expected to generate at leading order in gradients a comparably strong Néel-axis-locked interband absorptive anisotropy at leading order [34, 35]. By contrast, in an altermagnet, a distinct *texture-induced interband mechanism* is already available without intrinsic spin-orbit coupling because the altermagnetic low-energy doublet supports symmetry-allowed non-relativistic spin-split structure and momentum-dependent eigenvectors that feed directly into interband optical matrix elements.

Fig. 3 summarizes the optical fingerprint of a spin-helix texture. The overall lineshape of the total absorption $\mathfrak{A}(\omega)$, shown in Fig. 3(a), is controlled by the interband resonance condition, while the relative weight of its features depends strongly on the helix orientation ϕ_q . This angular dependence reflects that the relevant interband matrix elements are governed by the texture-induced mixing and its interference with the altermagnetic form factor.

Fig. 3(b) highlights two regimes separated by a crossover frequency ω_p . For $\omega \lesssim \omega_p$, the response is strongly polarization selective and $\mathfrak{D}(\omega) \approx 1$ over a broad window, indicating absorption dominated by a single linear polarization. In this *pinning regime*, the principal axis θ_+ develops plateaus and undergoes sharp $\pi/2$ reorientations as ϕ_q is varied. Near ω_p , $\mathfrak{D}(\omega)$ shows a pronounced dip accompanied by an abrupt $\pi/2$ rotation of θ_+ , signaling a narrow *crossover window* where the two eigenvalues of $M(\omega)$ become nearly degenerate. For $\omega \gtrsim \omega_p$ the response crosses over to a *tracking regime* in which $\theta_+(\omega)$ varies smoothly and approaches a helix-tracking law

$$\theta_+ \simeq \frac{\pi}{2} - \phi_q. \quad (24)$$

Fig. 4(a) makes the crossover at ω_p directly visible. The principal axis $\theta_+(\phi_q)$ follows the geometric tracking law in Eq. 24 (dashed line) once $\omega \gtrsim \omega_p$, whereas for $\omega \lesssim \omega_p$ it forms broad pinning plateaus separated by sharp $\pi/2$ switches.

This behavior can be understood by expressing the absorptive tensor in terms of interband matrix elements. Schematically, the interband contribution has the form

$$M_{ij}(\omega) \propto \int d\mathbf{k} |v_i^{+-}(\mathbf{k})| |v_j^{+-}(\mathbf{k})| W_\omega(\mathbf{k}), \quad (25)$$

where $W_\omega(\mathbf{k})$ is sharply peaked around the broadened resonance condition $\omega = E_+(\mathbf{k}) - E_-(\mathbf{k})$, with a width set by η and T .

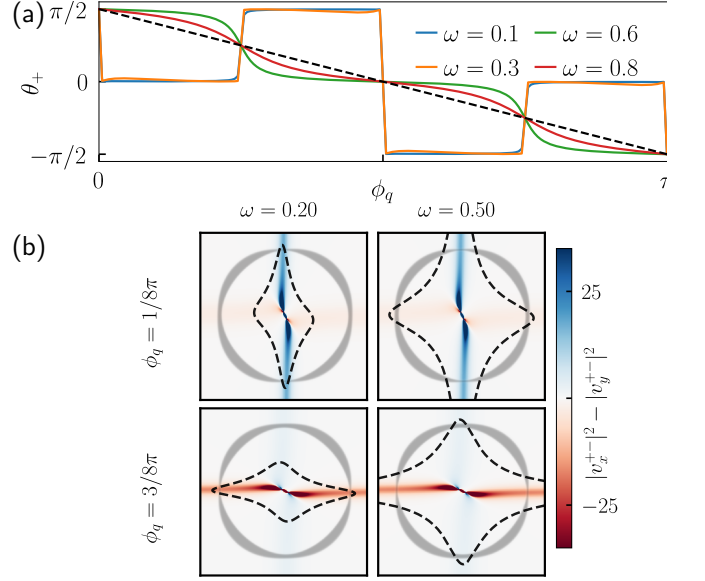


FIG. 4. (a) Principal absorption axis versus spiral direction for different frequencies. In the *pinning regime*, $\omega < \omega_p$, the principal absorption axis is pinned to be along the crystal axes, while for the *tracking regime*, $\omega > \omega_p$, the principal absorption axis tracks the helix direction. (b) Momentum-space origin of the dichroic response. The color map shows the anisotropic interband oscillator strength for two helix orientations (rows) and two probe frequencies ω (columns), as indicated in each panel. The black dashed contour marks the resonant condition $E_+(\mathbf{k}) - E_-(\mathbf{k}) = \omega$, while the thick gray circle indicates the Fermi surface of the underlying bands. The areas where the two meet is where $W_\omega(\mathbf{k})$ is nonzero.

Fig. 4(b) visualizes this weighting in momentum space. At high ω , the resonant weight samples the contour almost uniformly, so the resonance average becomes approximately $x \leftrightarrow y$ symmetric. In this regime, using Eq. (23), we can rewrite Eq. 25 as

$$M_{ij}(\omega) \propto q_i q_j \left\langle \frac{k_i^2 k_j^2}{d_1^2 + d_3^2} \right\rangle_{W_\omega}, \quad (26)$$

and $x \leftrightarrow y$ symmetric sampling implies the factorization

$$M(\omega) \propto \begin{pmatrix} q_y^2 & q_x q_y \\ q_x q_y & q_x^2 \end{pmatrix} = (q_y, q_x)(q_y, q_x)^T, \quad (27)$$

resulting in the tracking law in Eq. 24. Deviations for $\omega \lesssim \omega_p$ arise when $W_\omega(\mathbf{k})$ is dominated by anisotropic hot spots along the resonant contour, so that the averages in Eq. (26) are no longer approximately equal. In particular, for $\omega \ll \omega_p$ the weight concentrates near the crystal axes ($k_x \simeq 0$ or $k_y \simeq 0$), producing the $\pi/2$ switching regime.

Conclusions – We developed a minimal low energy theory for electrons moving in a smooth Néel texture in centrosymmetric collinear altermagnets. Working in the comoving frame, the texture enters through an SU(2) connection and generates three distinct structures that control the electronic response: an emergent U(1) gauge

coupling associated with topological defects, a texture metric term that acts as a scalar deformation, and a texture-induced pseudospin orbit coupling that is linear in the transverse connection. The application to a spin helix texture showed that it produces orientation dependent electronic signatures that reshapes the Fermi surface even in the absence of relativistic spin-orbit coupling. In linear response, it yields a tunable conductivity anisotropy and, most importantly, a strong polarization dependence of interband absorption. This leads to linear dichroism whose principal optical axes track the helix orientation, providing a direct and falsifiable route to detect and characterize textured altermagnetic states using polarization resolved optics.

This framework is flexible and opens several immediate directions. It applies to other altermagnetic symmetries by replacing the symmetry adapted form factors, and it

can be extended to include higher gradient terms and weak intrinsic spin orbit coupling. Time dependent textures provide an especially promising direction, where the same gauge fields enable genuinely dynamical optical and transport probes. More generally, domain walls and other inhomogeneous textures offer a route to engineer interface bound states [26, 27] and spatially controllable anisotropies. The same construction can be combined with superconducting proximity to access texture controlled Andreev spectra [36–39] together with magnetoelectric [40] and optoelectronic responses.

Acknowledgments – This work is funded by the Wallenberg Initiative on Networks and Quantum Information (WINQ). AM thanks Mikael Fogelström, Alberto Cortijo, and Ruben Seoane Souto for useful discussions.

Data availability – The code to reproduce the results of this paper can be found at Ref. [41].

[1] M. Naka, S. Hayami, H. Kusunose, Y. Yanagi, Y. Motome, and H. Seo, Spin current generation in organic antiferromagnets, *Nat. Commun.* **10**, 10.1038/s41467-019-12229-y (2019).

[2] M. Naka, S. Hayami, H. Kusunose, Y. Yanagi, Y. Motome, and H. Seo, Anomalous Hall effect in κ -type organic antiferromagnets, *Phys. Rev. B* **102**, 075112 (2020).

[3] L. Šmejkal, R. González-Hernández, T. Jungwirth, and J. Sinova, Crystal time-reversal symmetry breaking and spontaneous hall effect in collinear antiferromagnets, *Sci. Adv.* **6**, 10.1126/sciadv.aaz8809 (2020).

[4] I. Mazin, Editorial: Altermagnetism—a new punch line of fundamental magnetism, *Phys. Rev. X* **12**, 040002 (2022).

[5] L. Šmejkal, J. Sinova, and T. Jungwirth, Emerging Research Landscape of Altermagnetism, *Phys. Rev. X* **12**, 040501 (2022).

[6] T. Olsen, Antiferromagnetism in two-dimensional materials: progress and computational challenges, *2D Mater.* **11**, 033005 (2024).

[7] C. Autieri, New type of magnetism splits from convention, *Nature* **626**, 482 (2024).

[8] K.-H. Ahn, A. Hariki, K.-W. Lee, and J. Kuneš, Antiferromagnetism in RuO_2 d -wave Pomeranchuk instability, *Phys. Rev. B* **99**, 184432 (2019).

[9] H. Reichlova, R. Lopes Seeger, R. González-Hernández, I. Kounta, R. Schlitz, D. Kriegner, P. Ritzinger, M. Lammel, M. Leiviskä, A. Birk Hellenes, K. Olejník, V. Petříček, P. Doležal, L. Horak, E. Schmoranzerova, A. Badura, S. Bertaina, A. Thomas, V. Baltz, L. Michez, J. Sinova, S. T. B. Goennenwein, T. Jungwirth, and L. Šmejkal, Observation of a spontaneous anomalous hall response in the $mn5si3$ d -wave altermagnet candidate, *Nat. Commun.* **15**, 10.1038/s41467-024-48493-w (2024).

[10] J. Krempaský, L. Šmejkal, S. W. D’Souza, M. Hajlaoui, G. Springholz, K. Uhlířová, F. Alarab, P. C. Constantinou, V. Strocov, D. Usanov, W. R. Pudelko, R. González-Hernández, A. Birk Hellenes, Z. Jansa, H. Reichlova, Z. Šobáň, R. D. Gonzalez Betancourt, P. Wadley, J. Sinova, D. Kriegner, J. Minár, J. H. Dil, and T. Jungwirth, Altermagnetic lifting of Kramers spin degeneracy, *Nature* **626**, 517 (2024).

[11] S. Reimers, L. Odenbreit, L. Šmejkal, V. N. Strocov, P. Constantinou, A. B. Hellenes, R. Jaeschke Ubiergo, W. H. Campos, V. K. Bharadwaj, A. Chakraborty, T. Denneulin, W. Shi, R. E. Dunin-Borkowski, S. Das, M. Kläui, J. Sinova, and M. Jourdan, Direct observation of altermagnetic band splitting in $CrSb$ thin films, *Nat. Commun.* **15**, 10.1038/s41467-024-46476-5 (2024).

[12] R. M. Fernandes, V. S. de Carvalho, T. Birol, and R. G. Pereira, Topological transition from nodal to nodeless Zeeman splitting in altermagnets, *Phys. Rev. B* **109**, 024404 (2024).

[13] L. Šmejkal, J. Sinova, and T. Jungwirth, Beyond conventional ferromagnetism and antiferromagnetism: A phase with nonrelativistic spin and crystal rotation symmetry, *Phys. Rev. X* **12**, 031042 (2022).

[14] S. López-Moreno, A. H. Romero, J. Mejía-López, and A. Muñoz, First-principles study of pressure-induced structural phase transitions in MnF_2 , *Phys. Chem. Chem. Phys.* **18**, 33250 (2016).

[15] S. Lee, S. Lee, S. Jung, J. Jung, D. Kim, Y. Lee, B. Seok, J. Kim, B. G. Park, L. Šmejkal, C.-J. Kang, and C. Kim, Broken Kramers Degeneracy in Altermagnetic $MnTe$, *Phys. Rev. Lett.* **132**, 036702 (2024).

[16] T. Osumi, S. Souma, T. Aoyama, K. Yamauchi, A. Honma, K. Nakayama, T. Takahashi, K. Ohgushi, and T. Sato, Observation of a giant band splitting in altermagnetic $MnTe$, *Phys. Rev. B* **109**, 115102 (2024).

[17] B. Jiang, M. Hu, J. Bai, Z. Song, C. Mu, G. Qu, W. Li, W. Zhu, H. Pi, Z. Wei, Y.-J. Sun, Y. Huang, X. Zheng, Y. Peng, L. He, S. Li, J. Luo, Z. Li, G. Chen, H. Li, H. Weng, and T. Qian, A metallic room-temperature d -wave altermagnet, *Nat. Phys.* **21**, 754 (2025).

[18] M. Roig, A. Kreisel, Y. Yu, B. M. Andersen, and D. F. Agterberg, Minimal models for altermagnetism, *Phys. Rev. B* **110**, 144412 (2024).

[19] O. Gomonay, V. Baltz, A. Brataas, and Y. Tserkovnyak, Antiferromagnetic spin textures and dynamics, *Nat. Phys.* **14**, 213 (2018).

[20] H. Vakili, E. Schwartz, and A. A. Kovalev, Spin-transfer torque in altermagnets with magnetic textures, *Phys. Rev. Lett.* **134**, 176401 (2025).

[21] R.-C. Xiao, H. Li, H. Han, W. Gan, M. Yang, D.-F. Shao, S.-H. Zhang, Y. Gao, M. Tian, and J. Zhou, Anomalous-hall néel textures in altermagnetic materials, *Science China Physics, Mechanics, and Astronomy* **69**, [10.1007/s11433-025-2769-6](https://doi.org/10.1007/s11433-025-2769-6) (2025).

[22] O. J. Amin, A. Dal Din, E. Golias, Y. Niu, A. Zakharov, S. C. Fromage, C. J. B. Fields, S. L. Heywood, R. B. Cousins, F. Maccherozzi, J. Krempaský, J. H. Dil, D. Kriegner, B. Kiraly, R. P. Campion, A. W. Rushforth, K. W. Edmonds, S. S. Dhesi, L. Šmejkal, T. Jungwirth, and P. Wadley, Nanoscale imaging and control of altermagnetism in mnte, *Nature* **636**, 348 (2024).

[23] R. Yamamoto, L. A. Turnbull, M. Schmidt, J. C. C. Filho, H. J. Binger, M. D. P. Martínez, M. Weigand, S. Finizio, Y. Prots, G. M. Ferguson, U. Vool, S. Wintz, and C. Donnelly, *Altermagnetic nanotextures revealed in bulk mnte* (2025).

[24] G. Tatara, H. Kohno, and J. Shibata, Microscopic approach to current-driven domain wall dynamics, *Phys. Rep.* **468**, 213 (2008).

[25] G. Tatara, Effective gauge field theory of spintronics, *Phys. E: Low-Dimens. Syst. Nanostructures* **106**, 208 (2019).

[26] N. Davier and R. Ramazashvili, Texture-induced spin-orbit coupling and skyrmion-electron bound states in a néel antiferromagnet, *Phys. Rev. B* **107**, 014406 (2023).

[27] N. Davier and R. Ramazashvili, Electron states bound to a texture in a néel antiferromagnet, *Phys. Rev. B* **109**, 224425 (2024).

[28] T. Yokouchi, F. Kagawa, M. Hirschberger, Y. Otani, N. Nagaosa, and Y. Tokura, Emergent electromagnetic induction in a helical-spin magnet, *Nature* **586**, 232 (2020).

[29] P. F. Bessarab, D. Yudin, D. R. Gulevich, P. Wadley, M. Titov, and O. A. Tretiakov, Stability and lifetime of antiferromagnetic skyrmions, *Phys. Rev. B* **99**, 140411 (2019).

[30] O. Gomonay, V. P. Kravchuk, R. Jaeschke-Ubiergo, K. V. Yershov, T. Jungwirth, L. Šmejkal, J. v. d. Brink, and J. Sinova, Structure, control, and dynamics of altermagnetic textures, *npj Spintronics* **2**, [10.1038/s44306-024-00042-3](https://doi.org/10.1038/s44306-024-00042-3) (2024).

[31] P. Bruno, V. K. Dugaev, and M. Taillefumier, Topological hall effect and berry phase in magnetic nanostructures, *Phys. Rev. Lett.* **93**, 096806 (2004).

[32] M. Bode, M. Heide, K. von Bergmann, P. Ferriani, S. Heinze, G. Bihlmayer, A. Kubetzka, O. Pietzsch, S. Blügel, and R. Wiesendanger, Chiral magnetic order at surfaces driven by inversion asymmetry, *Nature* **447**, 190 (2007).

[33] V. Bonbien and A. Manchon, Symmetrized decomposition of the Kubo-Bastin formula, *Phys. Rev. B* **102**, 085113 (2020).

[34] P. Némec, M. Fiebig, T. Kampfrath, and A. V. Kimel, Antiferromagnetic opto-spintronics, *Nat. Phys.* **14**, 229 (2018).

[35] V. Grigorev, M. Filianina, S. Y. Bodnar, S. Sobolev, N. Bhattacharjee, S. Bommanaboyena, Y. Lytvynenko, Y. Skourski, D. Fuchs, M. Kläui, M. Jourdan, and J. Demsar, Optical Readout of the Néel Vector in the Metallic Antiferromagnet Mn₂Au, *Phys. Rev. Applied* **16**, 014037 (2021).

[36] S. S. Pershoguba, S. Nakosai, and A. V. Balatsky, Skyrmion-induced bound states in a superconductor, *Phys. Rev. B* **94**, 064513 (2016).

[37] C. W. J. Beenakker and T. Vakhtel, Phase-shifted Andreev levels in an altermagnet Josephson junction, *Phys. Rev. B* **108**, 075425 (2023).

[38] C. Sun, A. Brataas, and J. Linder, Andreev reflection in altermagnets, *Phys. Rev. B* **108**, 054511 (2023).

[39] A. Maiani and R. S. Souto, Impurity states in altermagnetic superconductors, *Phys. Rev. B* **111**, [10.1103/1541-0653/abf6nc](https://doi.org/10.1103/1541-0653/abf6nc) (2025).

[40] D. S. Rabinovich, I. V. Bobkova, A. M. Bobkov, and M. A. Silaev, Magnetoelectric effects in superconductor/ferromagnet bilayers, *Phys. Rev. B* **99**, 214501 (2019).

[41] A. Maiani, *Optical and transport anisotropies in spin-textured altermagnets: Code for the paper* (2026).

Appendix A: SU(2) theory of spin textures

To describe a smoothly varying Néel texture $\mathbf{n}(\mathbf{r})$, we perform a local SU(2) rotation that aligns the spin quantization axis with the exchange field. More precisely, we define a new local basis, i.e. the comoving frame, as a right-handed triad $(\mathbf{e}_1, \mathbf{e}_2, \mathbf{e}_3)$ where we identify $\mathbf{e}_3 = \mathbf{e}_1 \times \mathbf{e}_2 = \mathbf{n}$. Note that there is a local rotational freedom in choosing the unit vectors \mathbf{e}_1 and \mathbf{e}_2 ; this freedom corresponds to a residual $U(1)_z$ symmetry to be discussed later.

Basis change between the lab frame $(\mathbf{e}_x, \mathbf{e}_y, \mathbf{e}_z)$ and the comoving frame $(\mathbf{e}_1, \mathbf{e}_2, \mathbf{n})$ is implemented by a unitary in Eq. 3. Contextually, we define the SO(3) equivalent rotation as

$$R_{ij} = \frac{1}{2} \text{tr} [\sigma_i U \sigma_j U^\dagger] \quad (\text{A1})$$

The gauge field is defined as $\mathcal{A}_j = -iU^\dagger \partial_j U$ and can be decomposed as $\mathcal{A}_j = \mathbf{A}_j \cdot \boldsymbol{\sigma}/2$ where \mathbf{A}_i is a vector defined in the comoving frame. We can define the analogue potential in the lab frame as $\tilde{\mathbf{A}}_i = R\mathbf{A}_i$. In the following, we will assume to work in the comoving frame where $\mathbf{n} = \mathbf{e}_3$, therefore

$$R\partial_j \mathbf{n} = R\partial_\mu (R^{-1} \mathbf{e}_3) = R(\partial_\mu R^{-1}) \mathbf{e}_3 = \mathbf{A}_j \times \mathbf{n}. \quad (\text{A2})$$

By taking the cross product with \mathbf{n} , it follows the important relation

$$\mathbf{A}_j^\perp = \mathbf{A}_j - (\mathbf{A}_j \cdot \mathbf{n}) \mathbf{n} = \mathbf{n} \times \partial_j \mathbf{n}. \quad (\text{A3})$$

that establishes that the transverse component of the connection is entirely determined by the texture. For the longitudinal part, one can show that Eq. (A2) applies to any vector and thus $\partial_j \mathbf{e}_2 = \mathbf{A}_j \times \mathbf{e}_2$. Taking the scalar product with \mathbf{e}_1 and applying $\mathbf{e}_1 \times \mathbf{e}_2 = \mathbf{n}$ one gets to

$$A^\parallel = \mathbf{A}_j \cdot \mathbf{n} = -\mathbf{e}_1 \cdot \partial_j \mathbf{e}_2 \quad (\text{A4})$$

Since the definitions of \mathbf{e}_1 and \mathbf{e}_2 are arbitrary, this shows that the longitudinal component is controlled by the gauge freedom and can take any value. Only gauge-invariant combinations constructed from $\mathbf{n}(\mathbf{r})$ and its derivatives correspond to physical observables. A key example is the scalar

$$\mathbf{A}_j^\perp \cdot \mathbf{A}_k^\perp = \partial_j \mathbf{n} \cdot \partial_k \mathbf{n} \equiv g_{jk}, \quad (\text{A5})$$

which defines the energy tensor associated with spatial variations in \mathbf{n} . Physically, it measures the local deformation of the texture and coincides with the gradient energy density appearing in Heisenberg models. Other allowed couplings are $\mathbf{k}^\perp \cdot \boldsymbol{\sigma}^\perp$ and $(k - A^\parallel) \frac{\sigma^3}{2}$. Although the SU(2) gauge field is locally pure gauge, its curvature

$$\mathcal{F}_{jk} = \partial_j \mathcal{A}_k - \partial_k \mathcal{A}_j - i[\mathcal{A}_j, \mathcal{A}_k] \quad (\text{A6})$$

vanishes wherever $U(\mathbf{r})$ is smooth. Since $[D_j, D_k] = i\mathcal{F}_{jk}$, the covariant derivatives commute pointwise, and any nonzero field strength signals a gauge singularity (patching) associated with topological texture defects.

Projecting onto a fixed spin sector leaves an emergent Abelian gauge field $a_j \equiv A_j^\parallel/2$, with field strength

$$f_{jk} = \frac{1}{2} \left(\partial_j A_k^\parallel - \partial_k A_j^\parallel \right) = 2\pi \epsilon_{jk} \rho_s(\mathbf{r}), \quad (\text{A7})$$

where the skyrmion density is

$$\rho_s(\mathbf{r}) = \frac{1}{4\pi} \mathbf{n} \cdot (\partial_x \mathbf{n} \times \partial_y \mathbf{n}) = \frac{1}{4\pi} \mathbf{n} \cdot (\mathbf{A}_x^\perp \times \mathbf{A}_y^\perp). \quad (\text{A8})$$

Hence, the emergent flux $\int d^2r f_{xy} = 2\pi Q$ is quantized by the skyrmion number $Q = \int d^2r \rho_s$.

Appendix B: Schrieffer-Wolff treatment of arbitrary band structures

In this section, we treat a generic quartic band structure. To proceed, we expand the kinetic Hamiltonian around a generic inversion-invariant momentum \mathbf{k}_0 in the Brillouin zone. At such points, inversion symmetry ensures that the

full kinetic Hamiltonian is an even function of momentum. The Bloch Hamiltonian in the comoving frame then reads

$$\begin{aligned} H = & C^x \eta_x - J \sigma_z \eta_z \\ & + \sum_{\alpha \in \{0, x, z\}} \sum_{\substack{n=2 \\ \text{even}}}^{n_{\max}} \frac{(-i)^n}{n!} C_{a_1 \dots a_n}^{\alpha} \eta_{\alpha} \mathcal{W}[D_{a_1} \dots D_{a_n}] \\ & + \mathcal{O}(D^{n_{\max}+2}). \end{aligned} \quad (\text{B1})$$

The totally symmetric tensors $C_{a_1 \dots a_n}^{\alpha}$ are obtained from the Taylor expansion of the lattice dispersions $\varepsilon_{\alpha}(\mathbf{k})$ about an inversion-invariant momentum. Weyl ordering $\mathcal{W}[\dots]$ guarantees hermiticity and places every gauge-curvature commutator in the appropriate derivative order. For the quadratic part ($n = 2$) of the kinetic Hamiltonian, the Weyl symmetrization is automatically satisfied and explicit symmetrization only becomes necessary for higher-order ($n > 2$) dispersions such as d - or g -wave cases.

For $n = 2$ one has the symmetrized product $\frac{1}{2}\{D_j, D_k\}$, whose structure already reveals how spin textures generate scalar, gauge, and spin-orbit couplings in the low-energy theory. We start from this simpler case and then extend the reasoning to quartic order.

It is convenient to separate each covariant derivative into a longitudinal and a transverse component,

$$D_j^{\parallel} = \partial_j + i A_j^{\parallel} \frac{\sigma_z}{2}, \quad T_j = i \frac{\mathbf{A}_j^{\perp} \cdot \boldsymbol{\sigma}^{\perp}}{2}, \quad (\text{B2})$$

so that $D_j = D_j^{\parallel} + T_j$. Substituting into the anticommutator gives

$$\begin{aligned} \frac{1}{2}\{D_j, D_k\} = & \frac{1}{2}\{D_j^{\parallel}, D_k^{\parallel}\} \\ & + \frac{1}{2}(D_j^{\parallel} T_k + T_k D_j^{\parallel} + D_k^{\parallel} T_j + T_j D_k^{\parallel}) \\ & + \frac{1}{2}\{T_j, T_k\}. \end{aligned} \quad (\text{B3})$$

This identity already separates the three kinds of terms we want. The first term in Eq. (B3) is simplified by invoking the long-wavelength approximation, which allows longitudinal derivatives to act as commuting operators on smooth wavefunctions. Under this assumption, total derivatives are neglected (or boundary terms are assumed to vanish), and commutators $[D_a^{\parallel}, f]$ are suppressed by $(k_F L_{\text{txt}})^{-1}$. We then find

$$\frac{1}{2}\{D_j^{\parallel}, D_k^{\parallel}\} = (\partial_j + i A_j^{\parallel} \frac{\sigma_z}{2})(\partial_k + i A_k^{\parallel} \frac{\sigma_z}{2}), \quad (\text{B4})$$

which represents the *emergent electromagnetic coupling* to the Abelian gauge field A_j^{\parallel} . The terms with one T and one D^{\parallel} become

$$\begin{aligned} & \frac{1}{2}(D_j^{\parallel} T_k + T_k D_j^{\parallel} + D_k^{\parallel} T_j + T_j D_k^{\parallel}) \\ & = i(\mathbf{A}_j^{\perp} \partial_k + \mathbf{A}_k^{\perp} \partial_j) \cdot \frac{\boldsymbol{\sigma}^{\perp}}{2}, \end{aligned} \quad (\text{B5})$$

and represent precisely the *emergent pseudospin-orbit coupling* generated by the transverse texture. Finally, the purely transverse contribution reads

$$\frac{1}{2}\{T_j, T_k\} = -\frac{1}{4}(\mathbf{A}_j^{\perp} \cdot \mathbf{A}_k^{\perp}) \sigma_0 = -\frac{g_{jk}}{4}, \quad (\text{B6})$$

because the transverse Pauli matrices anticommute and $(\boldsymbol{\sigma}^{\perp})^2 = \sigma_0$ in the projected subspace. we see that this piece gives a *scalar potential* proportional to the texture metric.

We now turn to the fourth-order (quartic) symmetrized product of covariant derivatives, which appears in the long-wavelength expansion of higher-order dispersions. Such terms involve fully symmetrized products of the form

$$W[D_j D_k D_{\ell} D_m] = \frac{1}{4!} \sum_{\pi \in S_4} D_{\pi(j)} D_{\pi(k)} D_{\pi(\ell)} D_{\pi(m)}, \quad (\text{B7})$$

representing the Weyl-symmetrized covariant analogue of the quartic momentum term $k_j k_k k_\ell k_m$. Its expansion follows the same formal hierarchy as in the quadratic case but the physical distinction between “electromagnetic,” “spin-orbit,” and “scalar” contributions is no longer clear-cut. At this order, longitudinal derivatives appear in higher combinations and the texture-induced corrections intertwine with the kinetic tensor, so the decomposition is best regarded as an organizational scheme in powers of the transverse connection rather than a direct physical separation.

Keeping terms up to $(\mathbf{A}^\perp)^2$ we obtain

$$\begin{aligned} W[D_j D_k D_\ell D_m] &= D_j^\parallel D_k^\parallel D_\ell^\parallel D_m^\parallel \quad (B8) \\ &+ \frac{1}{4} \sum_{r \in \{j, k, \ell, m\}} \left(T_r \prod_{s \neq r} D_s^\parallel + \prod_{s \neq r} D_s^\parallel T_r \right) \\ &+ \frac{1}{4} \sum_{r < s} \{T_r, T_s\} \prod_{t \neq r, s} D_t^\parallel + \mathcal{O}((\mathbf{A}^\perp)^3). \end{aligned}$$

The truncation to second order in \mathbf{A}^\perp is then justified as follows. If the texture varies smoothly on a characteristic length L_{txt} , we have $|\partial_j \mathbf{n}| \sim 1/L_{\text{txt}}$, and the small parameter of the expansion is $k_F^{-1}/L_{\text{txt}} \ll 1$. Each extra power of the transverse connection $T_a \sim \partial_a \mathbf{n}$ carries an extra factor $1/(k_F L_{\text{txt}})$, so linear terms in A_j^\perp (emergent spin-orbit coupling) dominate, quadratic terms (metric potentials) are subleading, and cubic and higher terms become relevant only for rapidly varying textures.

At this point, we use the same simplification adopted in the quadratic case for the boundary term. With these simplifications, and collecting terms in the same way as for the quadratic operator, the fourth-order symmetrized product can be written in the transparent form

$$\begin{aligned} W[D_j D_k D_\ell D_m] &= D_j^\parallel D_k^\parallel D_\ell^\parallel D_m^\parallel + \frac{i}{8} \sum_r \left[(\mathbf{A}_r^\perp \cdot \boldsymbol{\sigma}^\perp) \prod_{s \neq r} D_s^\parallel + \prod_{s \neq r} D_s^\parallel (\mathbf{A}_r^\perp \cdot \boldsymbol{\sigma}^\perp) \right] \\ &- \frac{1}{16} \sum_{r < s} g_{rs} \sigma_0 \prod_{t \neq r, s} D_t^\parallel + \mathcal{O}((\mathbf{A}^\perp)^3). \quad (B9) \end{aligned}$$

Eq. (B9) is the exact analogue of Eq. (11) for quartic dispersions: the same three building blocks reappear, only dressed with the higher number of longitudinal derivatives appropriate to fourth order.

The symmetry of the sublattice matrices η_α determines the allowed structure of the tensors $C_{j_1 \dots j_n}^\alpha$ entering the long-wavelength expansion of the kinetic energy,

$$H_{\text{kin}} = \sum_{n=2,4,\dots} \frac{(-i)^n}{n!} C_{j_1 \dots j_n}^\alpha \eta_\alpha W[D_{j_1} \dots D_{j_n}], \quad (B10)$$

where the Weyl-symmetrized derivative products $W[\dots]$ ensure Hermiticity and gauge covariance. The lowest nontrivial tensor rank $n = 2$ produces the quadratic (*d*-wave) model discussed previously, while $n = 4$ corresponds to the quartic (*g*-wave) extension.

The matrix η_0 is invariant under all lattice symmetries, so it can only generate isotropic derivative tensors. This gives $C_{j_1 j_2 \dots j_n}^0 \propto \delta_{(j_1 j_2 \dots j_{n-1} j_n)}$, which is just the usual isotropic effective mass term.

The hybridization matrix η_x also yields an isotropic contribution in the lattices we consider, so its tensors take the same form,

$$C_{j_1 j_2 \dots j_n}^x = K^x \delta_{(j_1 j_2 \dots j_{n-1} j_n)}. \quad (B11)$$

As a result, η_0 and η_x only control the isotropic part of the low energy expansion.

The nontrivial angular structure comes from η_z . This term changes sign under sublattice interchange, and symmetry then restricts which derivative contractions can appear in C^z . These constraints determine whether the leading low energy form factor is of *d* wave type, *g* wave type, or higher.

For the *d* wave case on a tetragonal lattice, the leading allowed η_z contribution is quadratic and purely off diagonal in Cartesian indices,

$$C_{xy}^z = C_{yx}^z = K_d^z, \quad C_{xx}^z = C_{yy}^z = 0. \quad (B12)$$

Substituting these tensors into the general expansion and keeping terms up to second order reproduces the continuum Hamiltonian used in the main text.

For the g wave case, symmetry forbids a quadratic η_z term, so the first nonvanishing contribution appears at fourth order in derivatives. A minimal tetragonally allowed choice is

$$C_{xxyy}^z = C_{yyxx}^z = -C_{xyxy}^z = -C_{yxyx}^z = K_g^z, \quad (\text{B13})$$

with all other components zero. Contracting with Weyl symmetrized derivatives yields

$$C_{jklm}^z W[D_j D_k D_l D_m] = K_g^z W[D_x D_y (D_y^2 - D_x^2)], \quad (\text{B14})$$

which reduces to the continuum g wave form factor $k_x k_y (k_y^2 - k_x^2)$ in the texture free limit.

Retaining terms up to fourth order, the minimal long-wavelength Hamiltonian reads as

$$\begin{aligned} H_g = & C^x \eta_x - \frac{1}{2m} \eta_0 D^2 - \frac{K^x}{2} \eta_x D^2 \\ & + \frac{K_g^z}{4!} \eta_z W[D_x D_y (D_y^2 - D_x^2)] - J \sigma_z \eta_z. \end{aligned} \quad (\text{B15})$$

The quartic term produces a momentum dependence $k_x k_y (k_y^2 - k_x^2) \eta_z$, giving rise to a fourfold anisotropic spin splitting consistent with the g -wave representation. In the presence of a smooth Néel texture, the derivatives in Eq. (B15) are replaced by the covariant operators derived in the previous section, producing the corresponding gauge, spin-orbit, and scalar texture couplings for the g -wave case.

1. Low-energy effective theory

We consider the strong-coupling regime where the exchange scale J defines the dominant splitting, while the sublattice hybridization C^x is treated non-perturbatively together with J in the unperturbed Hamiltonian:

$$H = H_0 + V, \quad H_0 = C^x \eta_x - J \sigma_z \eta_z, \quad V = H_{\text{kin}} - C^x \eta_x. \quad (\text{B16})$$

Since $\{\eta_x, \eta_z\} = 0$ and $\sigma_z^2 = \eta_x^2 = \eta_z^2 = 1$, one has

$$H_0^2 = ((C^x)^2 + J^2) \mathbb{1} \equiv E_0^2 \mathbb{1}, \quad E_0 = \sqrt{J^2 + (C^x)^2}. \quad (\text{B17})$$

The low- and high-energy projectors (onto energies $\mp E_0$) therefore take the closed form

$$P = \frac{1}{2} \left(1 - \frac{H_0}{E_0} \right), \quad Q = 1 - P = \frac{1}{2} \left(1 + \frac{H_0}{E_0} \right). \quad (\text{B18})$$

It is convenient to parameterize the sublattice mixing by an angle ϑ ,

$$\cos \vartheta = \frac{J}{E_0}, \quad \sin \vartheta = \frac{C^x}{E_0}. \quad (\text{B19})$$

Inside the two-component subspace selected by P , we define a Pauli algebra by

$$\begin{aligned} \tau_0 &\equiv P(\eta_0 \sigma_0) P, & \tau_x &\equiv P(\eta_x \sigma_x) P, \\ \tau_y &\equiv P(\eta_x \sigma_y) P, & \tau_z &\equiv P(\eta_0 \sigma_z) P, \end{aligned} \quad (\text{B20})$$

with the additional useful projection identities

$$P \sigma_x P = -\sin \vartheta \tau_x, \quad P \sigma_y P = -\sin \vartheta \tau_y, \quad P \eta_x P = -\sin \vartheta \tau_0, \quad P \eta_z P = \cos \vartheta \tau_z, \quad P(\eta_z \sigma_{\perp}) P = 0, \quad (\text{B21})$$

and

$$P(\eta_y \sigma_x) P = \cos \vartheta \tau_y, \quad P(\eta_y \sigma_y) P = -\cos \vartheta \tau_x. \quad (\text{B22})$$

Note that several combinations that were nonzero in the full Hilbert space vanish after projection, e.g. $P \eta_y P = 0$ and $P(\eta_z \sigma_{\perp}) P = 0$.

To proceed, we decompose the kinetic perturbation into its three flavor channels and further separate each into spin-flipping and spin-preserving components:

$$V = V_{0,f} + V_{0,p} + V_{z,f} + V_{z,p} + V_{x,f} + V_{x,p}. \quad (\text{B23})$$

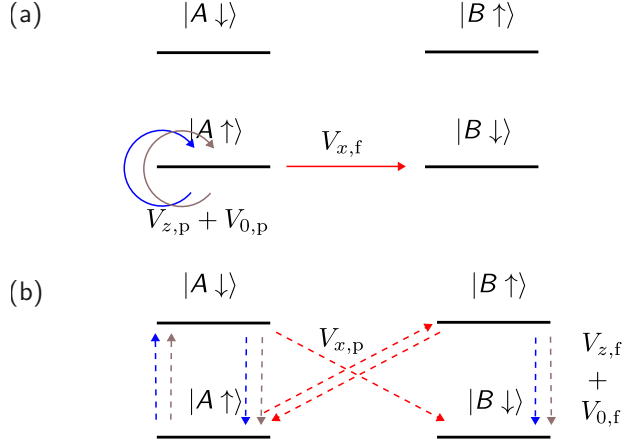


FIG. 5. Perturbative channels in the comoving-frame doublet. (a) First order: $V_{0,p}$ and $V_{z,p}$ act within a given spin sector, while $V_{x,f}$ flips the physical spin and couples the two doublets. (b) Second order: only channels with an even number of transverse flips survive upon projection, so the leading correction comes from the $\sigma_\perp\sigma_\perp$ processes built from $V_{0,f}$ and $V_{z,f}$, whereas diagonal $V_{x,p}$ terms are already contained in PHP .

At first order, only perturbations acting inside the low-energy doublet survive, i.e. PVP . In particular, in addition to the conventional spin-preserving terms ($V_{0,p}$ and $V_{z,p}$), there are two texture-induced contributions inside P : (i) the rank-2 η_x channel generates the universal pseudospin-orbit coupling term ($V_{x,f}$), and (ii) the isotropic η_0 channel contributes an additional pseudospin-orbit coupling term because $P\sigma_\perp P \neq 0$ once $C^x \neq 0$.

Neglecting the constant term $PH_0P = -E_0\tau_0$, the projected first-order Hamiltonian can be written compactly as

$$H_{\text{eff}}^{(1)} = PVP = +\frac{(C_{jk}^0 - \sin\vartheta C_{jk}^x)\tau_0 + (\cos\vartheta C_{jk}^z)\tau_z}{2} \left[\left(-i\partial_j + A_j^\parallel \frac{\tau_z}{2} \right) \left(-i\partial_k + A_k^\parallel \frac{\tau_z}{2} \right) + \frac{g_{jk}}{4} \tau_0 \right] - \frac{(C_{jk}^x - \sin\vartheta C_{jk}^0)}{2} \left[i(\mathbf{A}_j^\perp \partial_k + \mathbf{A}_k^\perp \partial_j) \cdot \frac{\boldsymbol{\tau}}{2} \right]. \quad (\text{B24})$$

Applying the construction just defined to derive the low-energy Hamiltonian for a spin-textured d -wave altermagnet returns

$$H_{d,\text{eff}} = \left(\frac{1}{2m} - \frac{K^x}{2} \sin\vartheta \right) \left[(-i\partial_x + A_x^\parallel \frac{\tau_z}{2})^2 + (-i\partial_y + A_y^\parallel \frac{\tau_z}{2})^2 + \frac{(\mathbf{A}_x^\perp)^2 + (\mathbf{A}_y^\perp)^2}{4} \tau_0 \right] - i \left(\frac{K^x}{2} - \frac{\sin\vartheta}{2m} \right) (\mathbf{A}_x^\perp \partial_x + \mathbf{A}_y^\perp \partial_y) \cdot \frac{\boldsymbol{\tau}}{2} + \frac{K_d^z \cos\vartheta}{2} \tau_z \left[-D_x^\parallel D_y^\parallel + \frac{g_{xy}}{2} \tau_0 \right] + \mathcal{O}((\mathbf{A}_\perp)^3). \quad (\text{B25})$$

which reduces to the expression in the main text for $C^x = 0$.

For the g -wave, we do the same, but we start from the rank-4 operator

$$+ \frac{K_g^z}{4!} \eta_z W [D_x D_y (D_y^2 - D_x^2)] \quad (\text{B26})$$

We now insert the quartic decomposition and only keep the pieces that survive the projection P . As in the d -wave case, all terms linear in the *transverse* gauge field carry a factor $\eta_z \sigma_\perp$, and therefore vanish under P because $P(\eta_z \sigma_\perp)P = 0$. What *does* survive are (i) the purely longitudinal quartic piece and (ii) the scalar/metric pieces $\propto g_{rs}\sigma_0$, because $P(\eta_z \sigma_0)P = \cos\vartheta \tau_z$. Therefore we obtain, after projection,

$$P \eta_z W [D_x D_y (D_y^2 - D_x^2)] P = \cos\vartheta \tau_z \left\{ D_x^\parallel D_y^\parallel [(D_y^\parallel)^2 - (D_x^\parallel)^2] - \frac{3}{16} \left[g_{xy} ((D_y^\parallel)^2 - (D_x^\parallel)^2) + (g_{yy} - g_{xx}) D_x^\parallel D_y^\parallel \right] \right\}. \quad (\text{B27})$$

Putting this together with the same isotropic quadratic piece and the rank-2 texture-induced pseudospin-orbit coupling, the *g-wave* analogue of Eq. (12) reads

$$\begin{aligned}
H_{g,\text{eff}} = & \left(\frac{1}{2m} - \frac{K^x}{2} \sin \vartheta \right) \left[(-i\partial_x + A_x^\parallel \frac{\tau_z}{2})^2 + (-i\partial_y + A_y^\parallel \frac{\tau_z}{2})^2 + \frac{(\mathbf{A}_x^\perp)^2 + (\mathbf{A}_y^\perp)^2}{4} \tau_0 \right] \\
& - i \left(\frac{K^x}{2} - \frac{\sin \vartheta}{2m} \right) (\mathbf{A}_x^\perp \partial_x + \mathbf{A}_y^\perp \partial_y) \cdot \frac{\boldsymbol{\tau}}{2} \\
& + \frac{K_g^z \cos \vartheta}{4!} \tau_z \left\{ D_x^\parallel D_y^\parallel [(D_y^\parallel)^2 - (D_x^\parallel)^2] - \frac{3}{16} [g_{xy}((D_y^\parallel)^2 - (D_x^\parallel)^2) + (g_{yy} - g_{xx}) D_x^\parallel D_y^\parallel] \right\} \\
& + \mathcal{O}((\mathbf{A}_\perp)^3).
\end{aligned} \tag{B28}$$

The structure of Eq. (B28) mirrors closely that of the *d-wave* model. The first line describes the isotropic k^2 dispersion dressed by the texture metric, while the second line is the universal texture-induced pseudospin-orbit coupling term generated by the rank-2 sector, with an additional contribution from the isotropic channel controlled by $\sin \vartheta$. The last line encodes the characteristic *g-wave* anisotropy with an overall reduction factor $\cos \vartheta = J/E_0$ arising from the projected η_z response.

2. Second-order terms for *d-wave* altermagnet

To second order in the SW expansion, the low-energy effective Hamiltonian is

$$H_{\text{eff}} = PH_0P + PVP - PVQ \frac{1}{2E_0} QVP + \mathcal{O}\left(\frac{V^3}{E_0^2}\right), \tag{B29}$$

where the gap between the low- and high-energy manifolds is $2E_0$.

In the strict long-wavelength truncation (keeping at most two spatial derivatives and up to $(\mathbf{A}^\perp)^2$), only the parts of V that are linear in σ_\perp are needed, since their square produces $(\mathbf{A}^\perp)^2$ corrections proportional to σ_0 . For the quadratic ($n = 2$) sector, it is convenient to define

$$\mathbf{B} \equiv \mathbf{A}_x^\perp \partial_x + \mathbf{A}_y^\perp \partial_y, \quad \mathbf{C} \equiv \mathbf{A}_x^\perp \partial_y + \mathbf{A}_y^\perp \partial_x. \tag{B30}$$

The corresponding spin-flip perturbations in the minimal k^2 theory are

$$V_{0,f} = -\frac{i}{2m} \eta_0 (\mathbf{B} \cdot \boldsymbol{\sigma}_\perp), \quad V_{z,f} = -\frac{iK_d^z}{4} \eta_z (\mathbf{C} \cdot \boldsymbol{\sigma}_\perp), \tag{B31}$$

where K_d^z denotes the quadratic η_z coefficient. The diagram in Fig. 5 suggests several second-order channels. However, after projecting onto the spin-aligned doublet, only processes with an *even* number of transverse spin-flip vertices contribute: mixed products involving a single σ_\perp vanish because $P\sigma_\perp P = 0$. Moreover, the ‘‘preserving’’ vertex $V_{x,p}$ is block-diagonal in the rotated spin basis and is already contained in PHP , rather than being generated perturbatively. As a result, in the present k^2 truncation the only nontrivial second-order contribution is the $\sigma_\perp-\sigma_\perp$ channel built from $V_{0,f}$ and $V_{z,f}$.

Using the long-wavelength contraction $(\mathbf{X} \cdot \boldsymbol{\sigma}_\perp)^2 \approx (\mathbf{X} \cdot \mathbf{X}) \sigma_0$ and the projection identities associated with the $H_0 = C^x \eta_x - J \sigma_z \eta_z$ splitting, one finds the second-order correction

$$\begin{aligned}
\Delta H_{A_\perp^2}^{(2)} = & -\frac{1}{2E_0} P(V_{0,f} + V_{z,f}) Q(V_{0,f} + V_{z,f}) P \\
\approx & \frac{\cos^2 \vartheta}{8m^2 E_0} (\mathbf{B} \cdot \mathbf{B}) \tau_0 + \frac{(K_d^z)^2}{32E_0} (\mathbf{C} \cdot \mathbf{C}) \tau_0 + \frac{K_d^z}{8mE_0} \cos \vartheta (\mathbf{B} \cdot \mathbf{C}) \tau_z.
\end{aligned} \tag{B32}$$

To express these terms explicitly at strict k^2 order, define $p_x = -i\partial_x$, $p_y = -i\partial_y$. Treating \mathbf{A}^\perp as slowly varying so that derivatives act primarily on the wavefunction, one has

$$\mathbf{B} \cdot \mathbf{B} \approx -[g_{xx}p_x^2 + g_{yy}p_y^2 + g_{xy}(p_x p_y + p_y p_x)], \tag{B33}$$

$$\mathbf{C} \cdot \mathbf{C} \approx -[g_{xx}p_y^2 + g_{yy}p_x^2 + g_{xy}(p_x p_y + p_y p_x)], \tag{B34}$$

$$\mathbf{B} \cdot \mathbf{C} \approx -[g_{xy}(p_x^2 + p_y^2) + (g_{xx} + g_{yy}) \frac{(p_x p_y + p_y p_x)}{2}]. \tag{B35}$$